Available online at www.sciencedirect.com
SCIENCE DIRECT
Earth and Planetary Science Letters 241 (2006) 634–647
EPSL
www.elsevier.com/locate/epsl

A three-dimensional Eulerian model for transport and deposition of volcanic ashes

A. Costa [a,*], G. Macedonio [a], A. Folch [b]

[a] *Istituto Nazionale di Geofisica e Vulcanologia-Osservatorio Vesuviano, Naples, Italy*
[b] *Institut de Ciències de la Terra "Jaume Almera" IJA-CSIC, Barcelona, Spain*

Received 20 July 2005; received in revised form 8 November 2005; accepted 9 November 2005
Available online 27 December 2005
Editor: S. King

Abstract

Volcanic ash fallout represents a serious threat to people living near active volcanoes because it can produce several undesirable effects such as collapse of roofs by ash loading, respiratory sickness, air traffic disruption, or damage to agriculture. The assessment of such volcanic risk is therefore an issue of vital importance for public safety and its mitigation often requires to evaluate the temporal evolution of the phenomenon through reliable computational models.

We develop an Eulerian model, named FALL3D, for the transport and deposition of volcanic ashes. The model is based on the advection–diffusion–sedimentation equation with a turbulent diffusion given by the gradient transport theory, a wind field obtained from a meteorological limited area model (LAM) and the source term derived from by buoyant plume theory. It can be used to forecast either ash concentration in the atmosphere or ash loading on the ground. Model inputs are topography, meteorological data given by a LAM, mass eruption rate, and a particle settling velocity distribution. A test application to the July 2001 Etna eruption is presented.

Keywords: volcanic ash transport; advection–diffusion–sedimentation equation; plume equations; particle dispersion; computational model; gradient transport theory

1. Introduction

Eruptive columns developed during explosive volcanic eruptions are able to inject large amounts of hot gases and ashes up to few tens of kilometres into the atmosphere. Volcanic ashes pose a risk to communities living around volcanoes because of several harmful effects such as collapse of roofs, respiratory sickness induced by ash inhalation, crop and livestock losses and risk to air traffic safety.

Eruptive columns commonly comprise three distinct regions characterised by different flow regimes: a lower basal gas-thrust or jet region, an intermediate convective region, and an upper umbrella region. Typically, the gas-thrust region extends only up to a small fraction of the total column height and it is characterised by a steep decrease of the gas–particle mixture velocity due to loss of momentum [1–3]. In contrast, the convective region is dominated by buoyancy forces acting on the hot erupted gases and heated entrained air. Physical models for this region are based on the buoyant plume theory [4] or on subsequent modifications of it

* Corresponding author. Present address: Department of Earth Sciences, University of Bristol, UK. Tel.: +44 117 954 5243; fax: +44 117 925 3385.
E-mail addresses: costa@ov.ingv.it (A. Costa), macedon@ov.ingv.it (G. Macedonio), afolch@ija.csic.es (A. Folch).

0012-821X/$ - see front matter © 2005 Elsevier B.V. All rights reserved.
doi:10.1016/j.epsl.2005.11.019

for volcanic ambit [5–10]. Finally, above the Neutral Buoyancy Level (NBL), the erupted material spreads under the effect of winds and atmospheric turbulence to form the umbrella region. Sizes of erupted particles may vary by several orders of magnitude, ranging from very fine sub-micron ash to clasts larger than one meter in diameter. The largest and heaviest particles leave the column at lower levels and follow complicated ballistic and non-ballistic trajectories [11], whereas the finest particles may remain entrapped by geostrophic winds for several years affecting the global climate. Particles within the intermediate size range are advected by wind, diffused by turbulence, settled by gravity and deposited finally on the ground at medium to distal distances. The latter group is the most important from the point of view of hazards.

Forecasting ash dispersion is a matter of fundamental importance for public safety in volcanic areas. To this purpose, it is essential to have models able to predict ground ash loading and atmospheric ash concentrations. Several families of models developed over the last few decades focus on particle settling and deposition in a wind field [12–15], turbulent atmospheric diffusion and advection by wind [16–22], particle dispersal from umbrella clouds which spread as gravity currents [23,24], and Lagrangian particle tracking [25–27]. However, none of these previous approaches incorporates relevant aspects such as real 3D wind fields, topographic effects, or adequate parameterisations for the turbulent atmospheric diffusion.

In this work we propose a 3D Eulerian model based on the advection–diffusion–sedimentation equation. The model uses a Limited Area Model (LAM) to evaluate the meteorological fields and the buoyant plume theory to describe the eruptive column. This approach leads to a more realistic treatment of volcanic ash transport and, for a given short-term meteorological and eruptive forecast, it has the potential capability to follow the evolution of particle concentration during the course of an eruption. The manuscript is organised as follows. Firstly, we present the physical formulation of the model, then we describe the numerical algorithm and, finally, as a first test-case, we apply the model to simulate the ash dispersion that occurred during the July 2001 Etna eruption.

2. Physical formulation

2.1. The advection–diffusion–sedimentation equation

Assuming that the main factors controlling atmospheric ash transport are wind advection, turbulent diffusion and gravity settling, and neglecting particle inertia and effects of particle–particle interaction, the continuity equation in an ordinary Cartesian system (x, y, z), for a particle settling velocity class with a given size d_j and a density ρ_{pj}, is:

$$\frac{\partial \bar{c}}{\partial t}+\frac{\partial u_x\bar{c}}{\partial x}+\frac{\partial u_y\bar{c}}{\partial y}+\frac{\partial u_z\bar{c}}{\partial z}-\frac{\partial v_{sj}\bar{c}}{\partial z}= -\frac{\partial \overline{u_x'c'}}{\partial x}-\frac{\partial \overline{u_y'c'}}{\partial y}-\frac{\partial \overline{u_z'c'}}{\partial z}+S \quad (1)$$

where $c(x,y,z,t)=\bar{c}+c'$ is the particle concentration, $(u_x,u_y,u_z)=(\bar{u}_x+u_x',\ \bar{u}_y+u_y',\ \bar{u}_z+u_z')$ is the wind velocity field, v_{sj} is the settling velocity of the considered class (actually its absolute value), and $S(x,y,z,t)$ is the mass concentration of particles brought into the domain per unit of time (source term). Terms with an over-bar represent the ensemble average part; that is, the sum of all the possible values at a time for all the possibilities of turbulent velocity [28], whereas terms with the 'prime' symbol indicate the turbulent fluctuations. According to the gradient transport theory (often also called "K-theory"), turbulent fluxes can be expressed in terms of average concentration gradients:

$$\overline{u_i'c'}=-K_j\frac{\partial \bar{c}}{\partial x_j} \quad (2)$$

where $K_j=x,y,z$ are the diagonal terms of the turbulent diffusivity tensor K. As in Toon et al. [29], Jacobson et al. [30], Park and Kim [31], we neglect the off-diagonal turbulent diffusion components. For a more general description including the off-diagonal components, see Byun and Chin [32]. Under this assumption, the non-conservative form of continuity Eq. (1) written in a generalised coordinate system (X, Y, Z) becomes:

$$\frac{\partial C}{\partial t}+U\frac{\partial C}{\partial X}+V\frac{\partial C}{\partial Y}+(W-V_{sj})\frac{\partial C}{\partial Z} = -C\nabla\cdot\mathbf{U}+C\frac{\partial V_{sj}}{\partial Z}\frac{\partial}{\partial X}\left(\rho_* K_X\frac{\partial C/\rho_*}{\partial X}\right)+\frac{\partial}{\partial Y}\left(\rho_* K_Y\frac{\partial C/\rho_*}{\partial Y}\right)+\frac{\partial}{\partial Z}\left(\rho_* K_Z\frac{\partial C/\rho_*}{\partial Z}\right)+S_* \quad (3)$$

where C is the scaled average concentration, (U, V, W) are the scaled wind speeds, K_X, K_Y and K_Z are the diagonal scaled diffusion coefficients, ρ_* the scaled atmospheric density and S_* is the source

term in the new coordinate system. Considering as a new frame of reference a simple terrain-following coordinate system where the horizontal coordinates remain unchanged ($x=X$, $y=Y$, $z\rightarrow Z$), the scaling factors are those reported in Table 1 (for more general transformations see e.g., Toon et al. [29]). Eq. (3) is solved for each particle velocity class independently, i.e., we assume no interaction between particles belonging to different classes during the transport process. This assumption is valid as long as particle concentration is sufficiently dilute, as it typically occurs in the umbrella region, although there is evidence that finer particles aggregate during their fall (see e.g., Cornell et al. [33]). We assume that finer particles aggregate immediately in the column region. For the sake of computational simplicity we do not consider particle aggregation during the transport process because it would couple equations for different classes resulting on a large increase of the computational time.

2.2. Meteorological fields

The rising of a volcanic eruption column into the atmosphere can strongly perturb the atmospheric wind field and the more intense the eruption, the stronger the perturbation is. However, the perturbative effect decreases with increasing distance from the vent. Since our purpose is to simulate atmospheric ash concentration and ash loading on the ground at medium to distal areas, we assume that the wind field remains unperturbed. This assumption should be valid at vent distances a few times larger than the column height. Wind field is obtained from mesoscale weather forecast models (e.g., LAMs based on the widely used MM5 [34] or RAMS [35] codes). LAMs are based on the solution of the standard non-hydrostatic Reynolds-averaged primitive equations, and typically involve horizontal spatial resolutions of about 5–10 km and variable vertical grid spacings from about 50 m near the surface to nearly one km at the upper layers. For instance, the non-hydrostatic Limited Area Model Italy (LAMI) used in Section 4, has a horizontal spatial resolution of 7 km and a temporal resolution of three hours. In general, length-scales involved in volcanic ash transport phenomena vary from few hundreds of metres to kilometres. Consequently, computational grids and temporal resolutions finer than those supplied by LAMs are normally required. For this reason, we use the mass consistent meteorological processor CALMET [36]. Assimilating topographic information (roughness and terrain heights e) and the meteorological output of a LAM on a coarse mesh, CALMET generates a zero-divergence wind field $\mathbf{U}=(U, V, W)$ on a finer grid using a terrain following coordinate system $X=x$, $Y=y$, $Z_*=z-e(x,y)$. In a first step, the initial guess wind field (in our case that given by a LAM) is adjusted for: (i) kinematic effects of terrain (lifting and acceleration of the air flow over terrain obstacles), (ii) thermodynamically generated slope flows, and (iii) blocking effects, in order to obtain, after a divergence-minimisation procedure, a Step 1 mass consistent wind field (U_1, V_1, W_1). After that, meteorological observations are added to the Step 1 field and an objective analysis procedure gives a second intermediate field (U_2, V_2, W_2). The scheme is designed so that observations are used to correct the Step 1 wind field within a user-specified radius of influence, whereas it remains unchanged in subregions where observations are unavailable. Finally, a new divergence-minimisation procedure is applied iteratively to (U_2, V_2, W_2) until the inequality:

$$\nabla\cdot\mathbf{U}<\epsilon \tag{4}$$

is satisfied (ϵ is a user-defined low bound). The final products of CALMET are a zero-divergence wind field consistent with the observations (or "pseudo-observations"), a finer scale interpolated temperature field and all the quantities needed in the parameterisation of the eddy diffusivity tensor such as the Monin–Obukhov length L, the friction velocity u_*, and the atmospheric boundary layer height h (see Section 2.3). The approximation of a zero-divergence wind field (4) is fully adequate at heights lower or close to one kilometre [37] although it is commonly extended up to few kilometres [38,31]. Therefore, the CALMET output field can be used directly only for low to medium eruptive columns whereas for high columns the assumption of anelastic atmosphere is more appropriate [37,39–41]:

$$\nabla\cdot(\rho_a\mathbf{U})<\epsilon \tag{5}$$

Table 1
Summary of the scaling factors for the terrain-following domain coordinate system ($x=X$, $y=Y$, $z\rightarrow Z$)

Parameter	Scaling
Coordinates	$X=x$, $Y=y$, $Z=z-h(x,y)$
Velocities	$U=u_x$, $V=u_y$, $W=u_zJ^{-1}$, $V_{sj}=v_{sj}J^{-1}$
Diffusion Coefficients	$K_X=K_x$, $K_Y=K_y$, $K_Z=K_zJ^{-2}$
Concentration	$C=c_J$
Density	$\rho_*=\rho J$
Source Term	$S_*=SJ$

J indicates the Jacobian of the coordinate system transformation.

(where ρ_a is the air density). In the latter case, a generalisation from (4) to (5) should be implemented in the CALMET model.

2.3. Parameterisation of the eddy diffusivity tensor

In order to solve Eq. (3) it is necessary to evaluate the vertical and horizontal diffusion coefficients. Inside the atmospheric surface layer, the Monin–Obukhov similarity theory estimates the vertical turbulent diffusivity K_z in terms of the friction velocity u_*, and the Monin–Obukhov length L:

$$K_z = \frac{\kappa z u_*}{\phi_h} \tag{6}$$

where κ is the von Karman constant ($\kappa = 0.4$), z is the distance from the ground, and ϕ_h is the atmospheric stability function (e.g., Jacobson [42]). Above the surface layer, the original form of the Monin–Obukhov similarity theory is no longer valid. In order to extend this theory to the entire boundary layer ($z/h < 1$) an evaluation of the Atmospheric Boundary Layer (ABL) height h is required. For this purpose, we use a simple parameterisation valid on the entire ABL [43]:

$$K_z = \begin{cases} \kappa u_* z\left(1-\dfrac{z}{h}\right)\left(1+9.2\dfrac{h}{L}\dfrac{z}{h}\right)^{-1} & h/L \geq 0 \text{ stable} \\ \kappa u_* z\left(1-\dfrac{z}{h}\right)\left(1-13\dfrac{h}{L}\dfrac{z}{h}\right)^{1/2} & h/L \leq 0 \text{ unstable} \end{cases} \tag{7}$$

Note that in the neutral case ($L \rightarrow \infty$) both expressions coincide. Finally, in the free atmosphere above the ABL ($z/h > 1$), K_z is considered a function of the local vertical wind gradient, a characteristic length scale l_c, and a stability function F_c depending on the Richardson number Ri:

$$K_z = l_c^2 \left|\frac{\partial V}{\partial z}\right| F_c(Ri) \tag{8}$$

For l_c and F_c we adopt the relationship used by the CAM3 model [44] of the National Center for Atmospheric Research (NCAR):

$$l_c = \left(\frac{1}{\kappa z} + \frac{1}{\lambda_c}\right)^{-1} \tag{9}$$

$$F_c(Ri) = \begin{cases} \dfrac{1}{1+10Ri(1+8Ri)} & \text{stable} \quad (Ri>0) \\ \sqrt{1-18Ri} & \text{unstable} \quad (Ri<0) \end{cases} \tag{10}$$

where λ_c is the so-called asymptotic length scale ($\lambda_c \approx 30$ m) while the Richardson number is calculated as $Ri = \frac{g}{\theta_v}\frac{\partial \theta_v/\partial z}{|\partial V/\partial z|^2}$ (with θ being virtual potential temperature).

On the other hand, for the horizontal eddy diffusivity $K_H = K_x = K_y$ we assume a large eddy parameterisation [45–49]:

$$K_H = \alpha \Delta x \Delta y \times \sqrt{\left(\frac{\partial v_x}{\partial y}+\frac{\partial v_y}{\partial x}\right)^2 + \frac{1}{2}\left[\left(\frac{\partial v_x}{\partial x}\right)^2 + \left(\frac{\partial v_y}{\partial y}\right)^2\right]} \tag{11}$$

where α is a dimensionless constant of the order of unity that ranges from 0.1 to 5 depending on the size of the domain, and Δx and Δy are the horizontal grid spacings. For our computational domains we set $\alpha = 0.5$.

Moreover, the model permits to use other K-parameterisations such as a constant value for K_z, a constant value for K_H or to estimate K_H using a Smagorinsky model as that used by RAMS model (for $\Delta z/\Delta = \ll 1$ [35]):

$$K_H = R_{max}\left(K_{mh}; (C_{SH}\Delta)^2 \sqrt{\left(\frac{\partial v_x}{\partial y}+\frac{\partial v_y}{\partial x}\right)^2 + 2\left[\left(\frac{\partial v_x}{\partial x}\right)^2 + \left(\frac{\partial v_y}{\partial y}\right)^2\right]}\right)$$
$$K_{mh} = 0.075 K_A \Delta^{4/3} \tag{12}$$

where $\Delta = \sqrt{\Delta_x \Delta_y}$, C_{SH} is a dimensionless constant ranging from 0.135 to 0.32, K_A is a user defined parameter close to one, and $R \simeq 3$.

2.4. Particle settling velocity model

Particle settling velocity is a crucial issue in any tephra transport model (e.g., Pfeiffer et al. [50]). In general, the atmospheric settling velocity of any particle is a complex function of its size d_j, sphericity Ψ (defined as the ratio of the surface of a sphere having the same particle volume to the actual particle surface), density ρ_{pj}, spatial orientation, plus air density ρ_a, and air viscosity η_a. However, semi-empirical expressions exist if one assumes that particles settle down at their terminal velocity (a reasonable assumption in the high atmosphere and fully valid elsewhere):

$$v_{sj}(z) = \sqrt{\frac{4 d_j \rho_{pj}}{3 C_D \rho_a}} \tag{13}$$

where C_D is the particle drag coefficient depending on the Reynolds number Re and sphericity Ψ. Settling velocities can only be computed approximately and strongly rely on semi-empirical evaluations of drag. A large number of experimental aerodynamic data are

available for certain regular and industrial shapes [51] but, unfortunately, measurements on the fall-velocities of volcanic particles are scarce; the most significant being Walker et al. [52] and Wilson and Huang [53]. Chhabra et al. [51] critically examined the performance of five different methods to evaluate the drag coefficient for non-spherical particles. The best fit appears to be that of Ganser [54] which gives the following expression for drag:

$$C_D = \frac{24}{ReK_i}\left\{1 + 0.1118[Re(K_1K_2)]^{0.6567}\right\} + \frac{0.4305K_2}{1 + \frac{0.4305}{ReK_1K_2}} \quad (14)$$

where $Re = \rho_a v_s d / \eta_a$ is the Reynolds number (d is the equivalent sphere volume diameter), and $K_1 = 3/(1+2\Psi^{-0.5})$ and $K_2 = 10^{1.84148(-\mathrm{Log}\Psi)0.5743}$ are two shape factors.

2.5. Definition of the source term: the eruptive column

In order to solve the advection–diffusion–sedimentation Eq. (3) it is necessary to evaluate the source term S (i.e., to estimate the mass per unit time released from the eruptive column at a given height). Commonly, ash dispersal models use a merely empirical mushroom-like shape for the column [16,50,55]. Instead, we derive the source term by coupling (3) with the buoyant plume theory equations that adequately describe the convective region of an eruptive column. In a still atmosphere, the steady, radial-averaged conservation equations for a volcanic plume containing N_ϕ particle classes are [9,10]:

$$\frac{d}{dz}\left(\pi r^2 \rho \hat{u}\right) = 2\pi r \rho_a u_e + \sum_{\phi=1}^{N_\phi} \frac{dM_\phi}{dz} \quad (15)$$

$$\frac{d}{dz}\left(\pi r^2 \rho \hat{u}^2\right) = \pi r^2 (\rho_a - \rho) g + \hat{u} \sum_{\phi=1}^{N_\phi} \frac{dM_\phi}{dz} \quad (16)$$

$$\frac{d}{dz}\left[\pi r^2 \rho \hat{u}\left(C_v T + gz + \frac{\hat{u}^2}{2}\right)\right] = 2\pi r \rho_a u_e \left(C_a T_a + gz + \frac{\hat{u}^2}{2}\right) + \left(C_p T + gz + \frac{\hat{u}^2}{2}\right) \sum_{\phi=1}^{N_\phi} \frac{dM_\phi}{dz} \quad (17)$$

where r is the radius of the axisymmetric plume at a given height z, ρ_a and ρ are, respectively, the density of the surrounding air and the density of the bulk (mixture of particles, volcanic gases and entrained air), $\hat{u}$ is the bulk averaged vertical velocity, u_e is the velocity of the entrained air (close to $0.15u$ according to laboratory experiments on tanks [10]), T is temperature, C_v is the bulk heat capacity of the material in the plume, C_a and C_p are the specific heats of air and pyroclasts, and M_ϕ is the mass of particles of size ϕ (i.e., $dM_\phi = dz$ gives the mass of particles fallen from the eruptive column). As usual, we assume that the mass of a given grain size fraction lost per unit of time is proportional to the amount of particles and to the terminal settling velocity [56]:

$$\frac{dM_\phi}{dz} = -\frac{\xi}{r\hat{u}} v_s(z,\phi) M_\phi; \quad \phi = 1 \ldots N_\phi \quad (18)$$

where ξ is an experimentally fitted parameter which should have a value of approximately 0.2. The above expression derives from tank experiments and theoretical models on dilute suspensions of particles in turbulent flows. Eqs. (15)–(18) constitute a set of $N_\phi + 3$ differential equations that give, for each height z, the bulk properties, the radius of the plume, and the mass of particles that leave the eruptive column per unit time (i.e., the source term at any height z). As input boundary conditions one only needs values for mass flow rate, vent exit velocity and temperature, and the bulk granulometric distribution of particles.

Eqs. (15)–(18) model the dynamics of the convective region of the column and should not be extended to the umbrella region. Above the NBL, we simply consider that the remaining mass is distributed between H_b (buoyancy level height) and H_c (total column height) following a Gaussian distribution in height, and that the column height is approximately given by $H_c = 1.43H_b$ [57]. It should be noted also that equations are constrained to the steady phases of an eruption. However, time dependency can be introduced as a succession of steady states whenever temporal variations occur smoothly (sustained eruptions). Once the column equations have been solved it simply remains to check which points of the FALL3D grid lie within the eruptive column domain and distribute the mass fallen accordingly, in order to obtain a source term for each particle class.

As in previous models (e.g., [16,50]), the size distribution of erupted material may be fitted using Rosin's probability density function:

$$f(\Phi) = \frac{1}{\sqrt{2\pi}\sigma_\Phi} \exp\left[-\frac{(\Phi - \Phi_\mu)^2}{2\sigma_\Phi^2}\right] \quad (19)$$

where $d=2^{-\Phi}$ mm is the particle diameter, Φ_u the median value and σ_Φ the standard deviation of the size distribution. Using this parameterisation for each type of component, we are able to describe the settling velocity spectrum with only two parameters for each component (Φ_u and σ_Φ). The bulk of the erupted mass is split into a user-defined number of grain-size and classes of components.

It is well known that finer ash particles attract each other while falling down because of electrostatic forces (e.g., Cornell et al. [33]). As stated previously, we assume no interaction among particles belonging to different classes during the transport process, but particle aggregation is simply considered assuming that, immediately in the source region, 50% particles belonging to the $\Phi=3$-class, 75% particles of $\Phi=4$-class and 100% of particle finer than $\Phi=5$-class settle as particle of $\Phi=2$-class with a density of 2000 kg/m^3 [33]. This approximation permits independent computations for each velocity class avoiding thus a sensible increase of the computational time.

3. Numerical algorithm

3.1. Space–time discretisation

Eq. (3) is solved using an explicit Finite Difference numerical algorithm:

$$\begin{aligned} C_{i,j,k}^{n+1} = C_{i,j,k}^{n} &- \Delta t\left(U\frac{\partial C}{\partial X}\right)_{i,j,k}^{n} - \Delta t\left(V\frac{\partial C}{\partial Y}\right)_{i,j,k}^{n} \\ &- \Delta t\left(W\frac{\partial C}{\partial Z}\right)_{i,j,k}^{n} + \Delta t\left(V_{sj}\frac{\partial C}{\partial Z}\right)_{i,j,k}^{n} \\ &- \Delta t(C\nabla\cdot\mathbf{U})_{i,j,k}^{n} + \Delta t\left(C\frac{\partial V_{sj}}{\partial Z}\right)_{i,j,k}^{n} + \Delta t\left(S_*\right)_{i,j,k}^{n} \\ &+ \Delta t\left(\frac{\partial}{\partial X}\left(K_{\mathrm{H}}\frac{\partial C}{\partial X}\right) + \frac{\partial}{\partial Y}\left(K_{\mathrm{H}}\frac{\partial C}{\partial Y}\right)\right)_{i,j,k}^{n} \\ &+ \Delta t\left(\frac{\partial}{\partial Z}\left(K_{\mathrm{V}}\frac{\partial C}{\partial Z}\right)\right)_{i,j,k}^{n} \end{aligned} \tag{20}$$

where subscripts indicate the spatial nodes and superscripts the temporal partition at the generic time instant $t^{\mathrm{n}}\in[t_{\mathrm{o}},t_{\mathrm{f}}]$ (t_{o} and t_{f} represent the initial and final time, respectively). Note that the term containing $\nabla\cdot\mathbf{U}$ vanishes if, as in our case, the wind field verifies Eq. (4).

The advective terms are discretised according to the Lax–Wendroff scheme which is second-order (see e.g., Ewing and Wang [58]). For instance, the advective term in the X-direction yields:

$$\begin{aligned} -\Delta t\left(U\frac{\partial C}{\partial X}\right)_{i,j,k}^{n} &= -\frac{Cr}{2}\left(C_{i+1,j,k}^{n} - C_{i-1,j,k}^{n}\right) \\ &\quad + \frac{Cr^2}{2}\left(C_{i+1,j,k}^{n} - 2C_{i,j,k}^{n} + C_{i-1,j,k}^{n}\right) \end{aligned} \tag{21}$$

where $\mathrm{Cr}=U\Delta t/\Delta x$ represents the Courant number (Δx is the horizontal grid spacing, assumed uniform, and Δt the computational time step). In order to reduce the numerical over- and under-shooting that commonly affects high-order schemes near discontinuities one can use slope limiter methods. In fact, these methods preserve the monotonicity of the solution while the accuracy remains higher than the first order upwind methods [59,60,58]. For instance, applying the minmod slope-limiter method and considering the general case with non-uniform velocity, Eq. (21) becomes:

$$\begin{aligned} -\Delta t\left(U\frac{\partial C}{\partial X}\right)_{i,j,k}^{n} &= -\frac{\Delta t}{\Delta x}\left(U_{i,j,k}^{n}C_{i,j,k}^{n} - U_{i-1,j,k}^{n}C_{i-1,j,k}^{n}\right) \\ &\quad - \frac{\Delta x}{2}\left[Cr_{i,j,k}^{n}\left(1-Cr_{i,j,k}^{n}\right)\sigma_{i,j,k}^{n}\right. \\ &\quad \left. - Cr_{i-1,j,k}^{n}\left(1-Cr_{i-1,j,k}^{n}\right)\sigma_{i-1,j,k}^{n}\right] \end{aligned} \tag{22}$$

where $\mathrm{Cr}_{i,j,k}^{n}=U_{i,j,k}^{n}\Delta t/\Delta x$, and:

$$\sigma_{i,j,k}^{n} = \mathrm{minmod}\left\{\frac{C_{i+1,j,k}^{n}-C_{i,j,k}^{n}}{\Delta x}, \frac{C_{i,j,k}^{n}-C_{i-1,j,k}^{n}}{\Delta x}\right\} \tag{23}$$

with $\mathrm{minmod}(a,\ b)=1/2(\mathrm{sgn}(a)+\mathrm{sgn}(b))\ \min(|a|,|b|)$ [58]. The introduction of other alternative limiter methods is straightforward.

The diffusive terms are evaluated using a central difference scheme accounting for a variable turbulent diffusivity tensor. Thus, for instance, the X-direction discretisation becomes:

$$\begin{aligned} &\left[\frac{\partial}{\partial X}\left(K_{\mathrm{H}}\frac{\partial C}{\partial X}\right)\right]_{i,j,k}^{n} \\ &= \frac{1}{2\Delta X^2}\left\{\left[K_{\mathrm{H},(i,j,k)} + K_{\mathrm{H},(i-1,j,k)}\right]C_{i-1,j,k}^{n} + \right. \\ &\quad - \left[K_{\mathrm{H},(i+1,j,k)} + 2K_{\mathrm{H},(i,j,k)} + K_{\mathrm{H},(i-1,j,k)}\right]C_{i,j,k}^{n} \\ &\quad \left. + \left[K_{\mathrm{H},(i+1,j,k)} + K_{\mathrm{H},(i,j,k)}\right]C_{i+1,j,k}^{n}\right\} \end{aligned} \tag{24}$$

The discretisations (22) and (24) are also used along the Y axis. However, they are generalised along the

vertical direction Z in order to account for the non-uniformity of the grid along the vertical direction.

The stability of the numerical scheme is ensured by using a time step Δt lower than the critical. As established by Hindmarsh et al. [61], an explicit scheme for the multidimensional advection–diffusion equation is numerically stable if the condition:

$$\Delta t \leq \frac{1}{\left[2\left(\frac{K_{\mathrm{H}}}{\Delta X^2}+\frac{K_H}{\Delta Y^2}+\frac{K_Z}{\Delta Z^2}\right)+\frac{U}{\Delta X}+\frac{V}{\Delta Y}+\frac{W}{\Delta Z}\right]} \quad (25)$$

is satisfied.

3.2. Boundary conditions and sedimentation

Free flow conditions were assumed at all boundaries of the computational domain. The choice of the boundary conditions is important in order to avoid absorption or reflection from these boundaries. In addition, we impose different boundary conditions for outgoing and incoming flux: for outgoing flux, zero derivative conditions, whereas for incoming flux, null concentrations at boundaries are assumed.

Particle sedimentation at the bottom face of the domain is calculated as the temporal integral of the outgoing mass flux from this surface. In this way, the mass loading per surface unit $L(X,Y)$, at the generic point (X,Y) and for a given particle class j, is given by:

$$L_j(X,Y,t_{\mathrm{k}}) = \int_{t_{\mathrm{o}}}^{t_{\mathrm{k}}} V_{sj}(X,Y,Z=0,t)C_j(X,Y,Z=0,t)\mathrm{d}t \quad (26)$$

where t_{o} represents the initial and t_{k} the generic time considered.

4. Application to the 2001 Etna eruption

Tephra fallout associated with the recent July–August 2001 and October 2002 Etna eruptions caused serious inconveniences to people living around the volcano and air traffic disruptions. For instance, during the July–August 2001 Etna eruption, flight operations were cancelled at Catania and Reggio Calabria airports [62]. The 2001 explosive activity from a vent at 2570 m a.s.l. comprised three main episodes: (i) phreatomagmatic explosions and tephra emission from 19 July to 24 July, (ii) Strombolian explosions and lava fountaining from 25–30 July and, (iii) a third episode similar to the first one, but less intense, lasting until 6 August [62]. As a preliminary application of the model, we simulated ash dispersal episodes occurred during the first eruptive phase. Since tephra fallout was negligible during 19 and 20 July, our simulation focuses only on the period from 21 July at 2 a.m. (GMT) to 25 July at 2 a.m., when copious ash fallout covered a large area around the volcano.

As part of a detailed description of the eruption, Scollo et al. [62] provides ash loading values and bulk grain-size distributions derived from deposit samples collected during 25–26 July, when no distal fallout occurred. Samples show a quasi-unimodal distribution ranging from lapilli to very fine ash. We used both ground ash loading measurements and particle size distribution data from Scollo et al. [62]. Data on particle size distribution were used as an input to Rosin's probability density function (19), i.e., they were used, together with the observed plume height, to infer the source term in Eq. (3) by means of the buoyant plume theory. It should be noted that bulk granulometric data from Scollo et al. [62] were inferred using the Voronoi tessellation method that, although better than other methods [63], must be viewed as an attempt to extrapolate the total grain size distribution. The best approach in our case should be to reconstruct the bulk settling velocity distribution directly by best-fit with field data. The solution of this inverse problem would require very large computational times unless a parallel version of the code is used. However, this will be the subject of a further paper (in preparation).

Ground ash loading measurements allowed us to validate the model confronting, its predictions to field observations. We considered up to 7 particle classes ranging from $\phi \leq 0$ to $\phi \geq 6$ (see Table 2). For the finest particle classes having a diameter smaller than $\phi = 5$, we consider as representative only one particle class with a total mass percentage of the order of 1% and a diameter of about 15 μm which corresponds to typical effective particle diameters of Mt. Etna aerosol plumes as inferred from photometric observations [64,65]. Most of the mass (75% approximately) concentrates at the upper part of the column (from ~1500 to 2500 m above the vent), but this value obviously depends on the particle size because large clasts leave the column at lower levels and the finest particles concentrate almost completely at the upper part.

Table 3 summarises other input data used in the simulations. We assume a plume of average height 4770 m a.s.l. (2200 m above the vent). This value results from averaging the 4500 m observed during 21–22 July and the 5000 m during 23–24 July. In order to reproduce this column height with the plume Eqs. (16)–(18), and considering a vent diameter of about 50 m, one needs an exit velocity of 50–60 m/s and a mass flow rate of

Table 2
Grain-size distributions reported by Scollo et al. [62] (left) and used in simulations (right)

Bulk distribution from Scollo et al. [62]			Bulk distribution used in the simulation			
ϕ	Diameter (mm)	Weight (%)	Class	ϕ	Density (kg/m^3)	Weight (%)
−3	8	0.02	–	–	–	–
−2	4	0.14	–	–	–	–
−1	2	0.54	–	–	–	–
0	1	1.71	1	≤0	1500	2.41
1	0.5	5.83	2	1	1500	5.83
2	0.25	33.46	3	2	2000	33.46
3	0.125	46.00	4	3	2000	45.00
4	0.0625	11.15	5	4	2500	11.15
5	0.02	1.14	6	5	2500	1.15
	0.003	–	7	≥6	2500	1.00

Simulation considers up to seven particle classes ranging from $\phi \leq 0$ to $\phi \geq 6$.

7×10^3 kg/s. It should be noted that, despite the fact that plume model is more adequate for larger Plinian and sub-Plinian eruptive columns, the predicted results are consistent with observations even for the case of a short plume such the one considered here. For instance, a constant averaged mass flow rate of 7×10^3 kg/s sustained during the 96 h of the simulation yields a total erupted mass of ~2.4×10^9 kg. This value in excellent agreement with the 2.3×10^9 kg derived by Scollo et al. [62] from the power law fit on the semi-logarithmic plot of mass per area unit versus $\sqrt{Area}$.

Meteorological field (wind and temperature) and meteorological parameters (friction velocity, boundary layer height, etc.) were calculated using the meteorological processor CALMET considering, as large scale prognostic field input, the non-hydrostatic Limited Area Model Italy (LAMI), which has a horizontal spatial resolution of 7 km and a temporal one of three hours (see e.g., Barsotti et al. [66]). We used two different computational domains of size $100 \times 100 \times 4$ km and $300 \times 300 \times 4$ km. The smaller domain has a higher horizontal resolution to compute ground ash loading more accurately, whereas the larger domain serves to track the trajectories of aerosols and finer particles at large distances from the source. Both domains are built up with 15 vertical layers and horizontal spatial resolutions of 1 and 2 km, respectively (i.e., meshes have 150,000 and 337,500 nodal points). The vertical grid spacing is quite variable and ranges from 10 m at the lower layer to 500 m at the upper one. We used a finer mesh near the ground in order to capture the characteristics of the ABL, which define the vertical diffusivity tensor according to the K-theory. A novel aspect of this model is that the values of the diffusion coefficients are directly computed from meteorological data and, consequently, vary from point to point and from time to time. In this particular application, values for vertical diffusivity K_z range from ~5×10^{-5} to ~100 m^2/s, whereas those for horizontal diffusion range from ~100 to ~10^4 m^2/s.

Table 3
Parameters used to simulate Etna ash dispersal from 21 to 24 July 2001

Parameter	(Unit)	Value
Vent coordinates	(UTM)	(500,352; 4,176,302)
Vent elevation	(m)	2570
Vent diameter	(m)	50
Exit velocity	(m/s)	55
21–24 July averaged column height*	(m)	≈ 2200
21–24 July averaged mass flow rate**	(kg/s)	7×10^3
Meteorological Input Data		LAMI

*Average from the ≈ 2000 m observed during 21–22 and the ≈ 2500 m during 23–24. **Best value to reproduce the column height using the plume model. Should be understood as a mean value during 96 h. The corresponding erupted mass is 2.4×10^9 kg.

The simulations are able to reproduce main features of the deposit such as the isomass lines (including the bilobate shape), or the ϕ-mode variation of the samples from $\phi = 1$ at 0–4 km to $\phi = 2$–3 afterwards. Fig. 1 plots, for different time slices, vertical sections along the X–Y axis passing through the vent. Computed ground ash load contours at the end of the simulated period are plotted in Fig. 2, where field samples from Scollo et al. [62] are also shown for comparison. We have selected 42 sample points excluding only those that were very close to the source (≤5 km corresponding to two times the column height). It would be noted that, generally, Eulerian models are more suitable at large distances from the source, whereas Lagrangian descriptions work better in regions very close to the source [48]. For these reasons the best

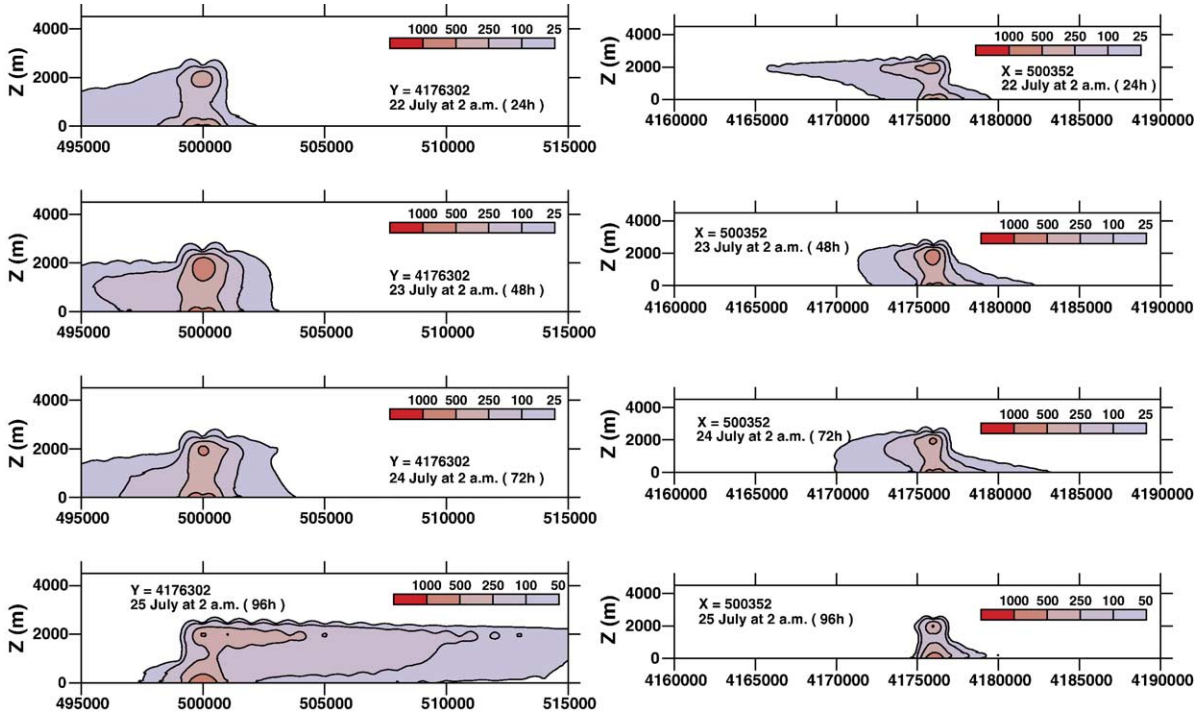

Fig. 1. Vertical sections showing concentration (in 10^{-3} g/m^3) at different time instants (UTM coordinates are used). Left: sections at constant Y (Y=4,176,302 m). Right: sections at constant X (X=500,352 m). In both cases, the corresponding time instants are, from top to bottom, 24, 48, 72, and 96 h, respectively.

approach should be hybrid, working as a Lagrangian model in the proximal region and as a Eulerian model in the distal part.

The results of simulations show that this model can, without need of any "ad hoc" parameter, reproduce realistic shapes of the isopachs different from the sim-

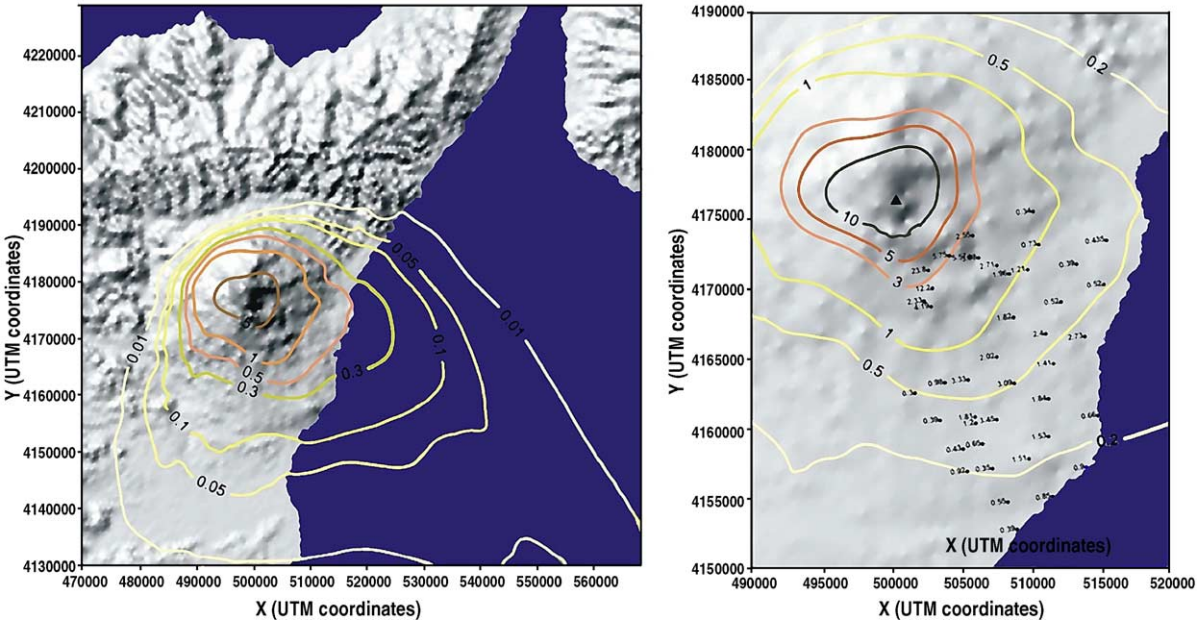

Fig. 2. Left: computed isomass contours (in kg/m^2) after 96 h of simulation. Right: close up view near the vent (triangle) showing also the location and the value of the 42 selected field data points.

pler elliptical-like isolines obtained by semi-analytical models such as HAZMAP (see Scollo et al. [62]). Note that simplified semi-analytical models, such as HAZMAP [55] or TEPHRA [67], are not suitable to study ash dispersal in the ABL. Punctual measurements and values computed on the corresponding computational cells are reported in Fig. 3 where a semi-quantitative accord is shown. As observed from this figure agreement is generally acceptable (the correlation coefficient is 0.72, more than 80% of the computed points are within 1/5 and 5 times the observed values) specially at distances from 5–15 km, but larger differences exist in the most distal region probably because the deposit at greater distances contains mainly fine particles, for which granulometry has been oversimplified in the simulations (one single class for $\phi \geq 6$), and for which uncertainty on the mass fraction is large. Secondly, the comparison of the thinner punctual measured values with those simulated on the computational cells cannot be very representative because of the spatial variations. As stated previously, a parallel version of the code can be used to obtain the bulk settling velocity distribution directly by best fit with field data. Preliminary results by using this approach show a sensible improvement in reconstructing the observed ash deposits indicating the general inadequacy of the assumed bulk granulometric distribution.

Another qualitative way to validate the model is through comparison with satellite images. Fig. 4 compares results with some satellite images taken at different time slices (July 22 at 7 a.m. and July 24 at 10 a.m.) and illustrates how the model is able to track quite accurately the position and extension of the plume. Apart from computing results on the ground, another important feature of the model is that it can also predict time evolution of concentration in the air. It allows, for instance, to determine where/when flight operations may become unsafe. Just to illustrate, Fig. 5 plots concentration levels at 1 and 2 km above the ground for different time slices. Assuming 10^{-3} g/m^3 as a concentration threshold for flight safety, the contours in the figure bound the unsafe region for the considered height.

5. Summary and discussion

We have developed a three-dimensional Eulerian model, named FALL3D, for the atmospheric transport

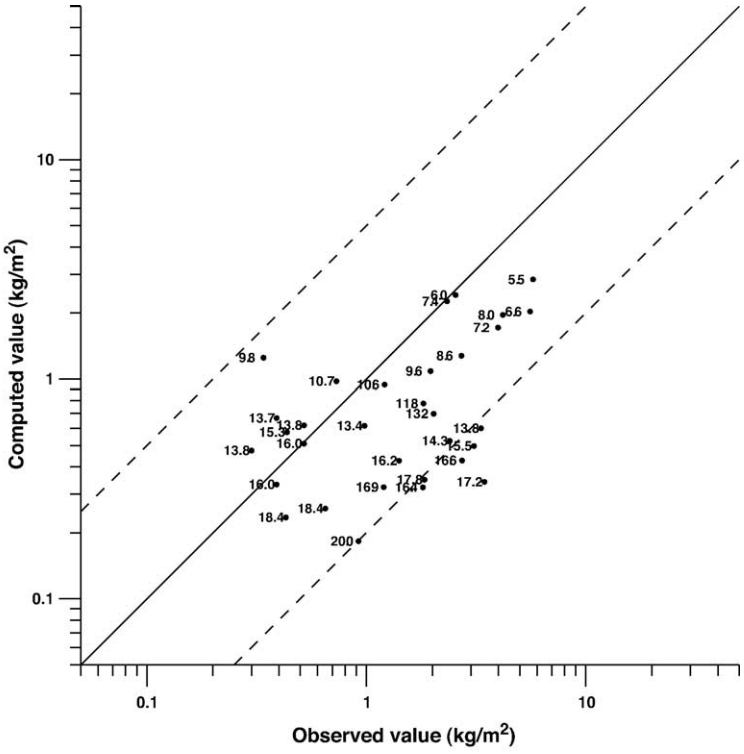

Fig. 3. Comparison between punctual measured data and values obtained by simulation on the corresponding cell of the computational grid. The correlation coefficient is 0.72. Numbers at each of the 42 points indicate radial distance to the vent. Dotted lines indicate over- or under-estimations of both 1/5 and 5 times the observed values.

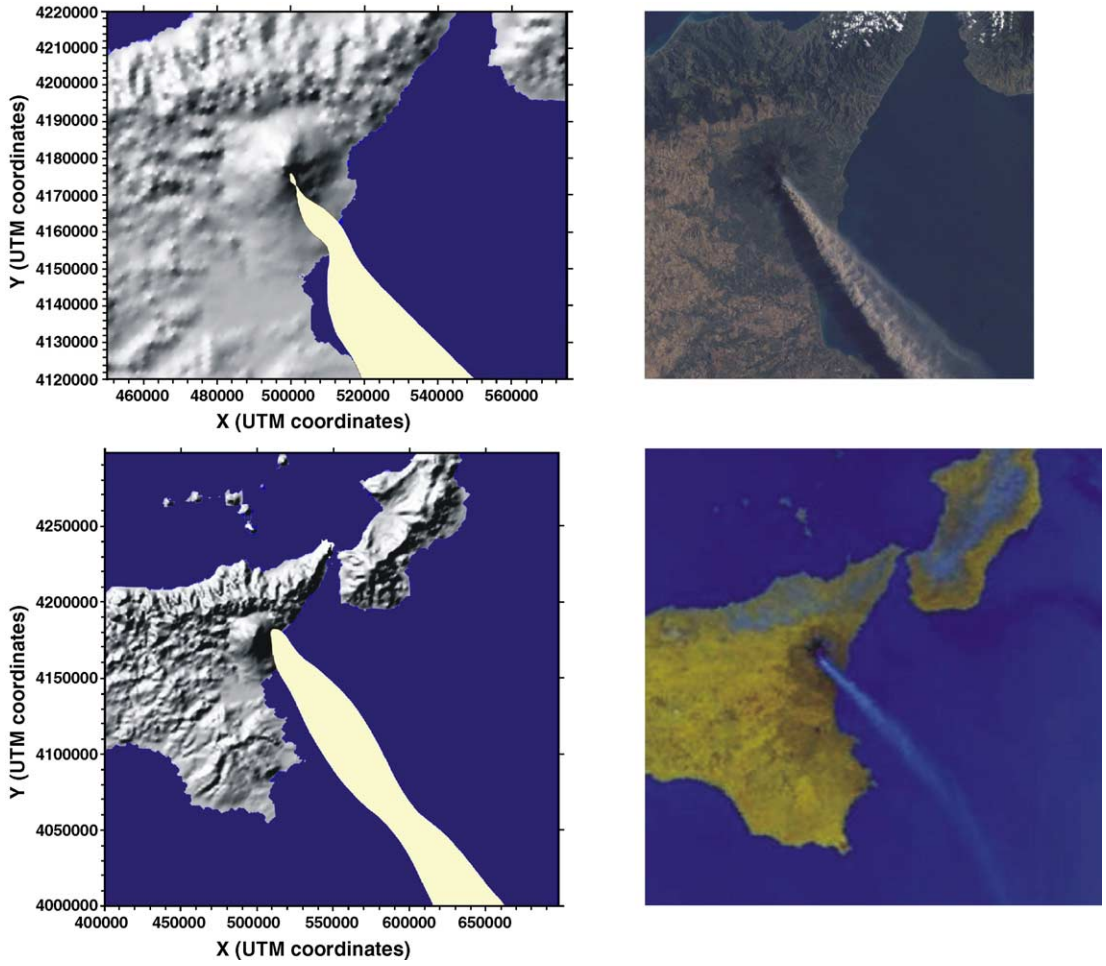

Fig. 4. Comparison between numerical results and a satellite images at 22 July 7 a.m. (top) and 24 July at 10 a.m. (bottom). Numerical results are shown at a height of 3 km. Contours indicate a concentration of 3×10^{-6} g/m^3. Multiplying this concentration by the optical depth one gets the value assumed as the lower visual threshold.

and deposition of volcanic ashes. From a computational point of view, the model has a modular structure that easily permits the user to modify the used parameterisations or to implement new ones. Relevant and novel features of this transport model are: (i) it is coupled with a meteorological forecast, (ii) it accounts for terrain effects, (iii) it incorporates a realistic evaluation of turbulent atmospheric diffusion based on the K-theory, and (iv) it derives the source term from the buoyant plume theory. This last feature allows a continuous spatial distribution of sources, different for each particle class, which eventually, may also vary with time. The use of realistic 3D wind fields and the assessment of the source terms is an important step towards more accurate predictions of volcanic ash fallout. However, meteorological and plume couplings still present two major limitations in the current version. Firstly, the meteorological processor should be generalised to the case of an anelastic atmosphere if one aims to model particle dispersion from large eruptive columns (Plinian eruptions). Secondly, the local perturbations that the column induces on the wind field should be also incorporated since these may affect model predictions at proximal to intermediate distances. Again, the larger the column, the higher the perturbation is expected to be.

A preliminary application of FALL3D to the 2001 Etna eruption has shown the ability of the model to reproduce realistic field data and plume patterns observed from satellites without using any “ad hoc” parameters and assuming a total grain size distribution obtained by a completely different method (a parallel version of the code can permit reconstruction of the bulk granulometric distribution directly from field data by best fitting).

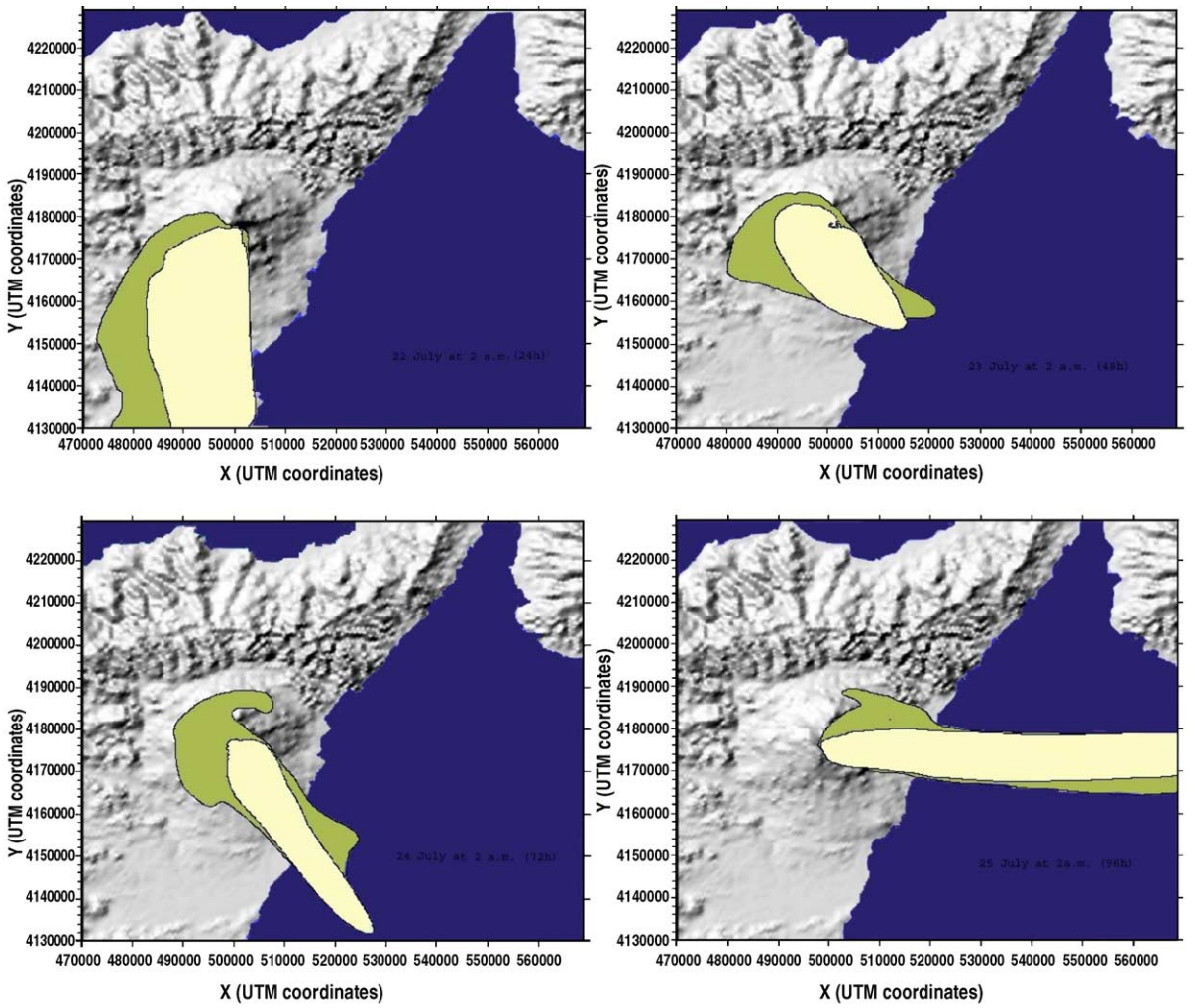

Fig. 5. Horizontal sections at 1 (lower brown colour) and 2 km (upper cream colour) above the ground at 24, 48, 72, and 96 h after the onset of the eruption. The levels correspond to concentrations of 1×10^{-3} g/m^3, a value considered as the limit above which aircrafts cannot fly.

Moreover, the performance of the model can be increased by improving the used parameterisations, better calibrating some parameter values and introducing important feedback coupling between volcanic column and atmosphere. Characteristic computing times running on an ordinary Pentium-4 desktop using a 150,000 node mesh and 7 particle classes, are 8 h of CPU per day of simulation. This 1:3 factor is, nevertheless, quite variable because it depends on the critical time step, i.e., on the wind velocity and diffusivity values. Clearly these computing times may be acceptable to study past events, but render the code unpractical during an emergency situation. In order to overcome this limitation, a parallel version of the code will be completed soon. The increase in computational performance of the parallel version will also permit better the constrain of the physical parameterisations by reconstructing well described eruptions and eventually the use of the model during future eruptions.

Acknowledgements

This work was supported by the EU Research Project EXPLORIS N. EVR1-2001-00047 and the HPC-EUROPE Transnational Access Program. We wish to thank S. Scollo to provide the July 2001 Etna eruption data, S. Barsotti for her help in the elaboration of the meteorological data. C. Cavazzoni and G. Erbacci from CINECA (Bologna, Italy) are acknowledged for their support on the code implementation.

References

[1] S. Kieffer, Factors governing the structure of volcanic jets, Explosive Volcanism: Inception, Evolution and Hazards, National Academy Press, Washington DC, 1984, pp. 143–157.

[2] S. Kieffer, B. Sturtevant, Laboratory studies of volcanic jets, J. Geophys. Res. 89 (1984) 8253–8268.

[3] F. Dobran, A. Neri, G. Macedonio, Numerical simulation of collapsing volcanic columns, J. Geophys. Res. 98 (B3) (1993) 4231–4259.

[4] B. Morton, G. Taylor, J. Turner, Turbulent gravitational convection from mantained and instantaneous sources, Proc. R. Soc. Lond., Ser. A 234 (1956) 1–23.

[5] L. Wilson, Explosive volcanic eruptions. III. Plinian eruption columns, Geophys. J. R. Astron. Soc. 45 (1976) 543–556.

[6] L. Wilson, R. Sparks, T. Huang, N. Watkins, The control of volcanic column heights by eruption energetics and dynamics, J. Geophys. Res. 83 (1978) 1829–1836.

[7] R. Sparks, L. Wilson, Explosive volcanic eruptions — V. Observations of plume dynamics during the 1979 Soufrière eruption, St. Vincent, Geophys. J. R. Astron. Soc. 69 (1982) 551–570.

[8] R. Sparks, The dimensions and dynamics of volcanic eruption columns, Bull. Volcanol. 48 (1986) 3–15.

[9] A. Woods, M. Bursik, Particle fallout, thermal disequilibrium and volcanic plumes, Bull. Volcanol. 53 (1991) 559–570.

[10] M. Bursik, Effect of wind on the rise height of volcanic plumes, Geophys. Res. Lett. 18 (2001) 3621–3624.

[11] S. Lo Savio, 2004. Modelling the dynamics of large particles in explosive eruptions. Ph.D. thesis, University of Bologna, Bologna.

[12] S. Carey, H. Sigurdsson, Influence of particle aggregation on deposition of distal tephra from the May 18, 1980, eruption of Mount St-Helens volcano, J. Geophys. Res. 87 (B8) (1982) 7061–7072.

[13] S. Carey, R. Sparks, Quantitative models of the fallout and dispersal of tephra from volcanic eruption columns, Bull. Volcanol. 48 (1986) 109–125.

[14] M. Bursik, R. Sparks, J. Gilbert, S. Carey, Sedimentation of tephra by volcanic plumes. I. Theory and its comparison with a study of the Fogo A Plinian deposit São Miguel (Azores), Bull. Volcanol. 54 (1992) 329–344.

[15] C. Bonadonna, G. Ernst, R. Sparks, Thickness variations and volume estimates of tephra fall deposits: the importance of particle Reynolds number, J. Volcanol. Geotherm. Res. 81 (1998) 173–187.

[16] T. Suzuki, A theoretical model for dispersion of tephra, in: D. Shimozuru, I. Yokoyama (Eds.), Arc Volcanism: Physics and Tectonics, Terra Scientific Publishing Company (TERRAPUB), Tokyo, 1983, pp. 93–113.

[17] P. Armienti, G. Macedonio, M. Pareschi, A numerical model for the simulation of tephra transport and deposition: applications to May 18, 1980, Mt. St. Helens eruption, J. Geophys. Res. 93 (B6) (1988) 6463–6476.

[18] G. Macedonio, M. Pareschi, R. Santacroce, A numerical simulation of the Plinian fall phase of the 79 AD eruption of Vesuvius, J. Geophys. Res. 93 (B12) (1988) 14817–14827.

[19] L. Glaze, S. Self, Ashfall dispersal for the 16 September 1986 eruption of Lascar, Chile, calculated by a turbulent diffusion model, Geophys. Res. Lett. 18 (1991) 1237–1240.

[20] C. Connor, B. Hill, B. Winfrey, M. Franklin, P. La Femina, Estimation of volcanic hazards from tephra fallout, Nat. Hazards Rev. 2 (2001) 33–42.

[21] C. Bonadonna, G. Macedonio, R. Sparks, Numerical modelling of tephra fallout associated with dome collapses and Vulcanian explosions: application to hazard assessment on Montserrat, in: T. Druitt, B. Kokelaar (Eds.), The Eruption of Soufriére Hills Volcano, Montserrat, from 1995 to 1999, Geol. Soc. Lond., 2002, pp. 517–537.

[22] A. Folch, A. Felpeto, A coupled model for the dispersal of tephra during sustained explosive eruptions, J. Volcanol. Geotherm. Res. 145 (3–4) (2005) 337–349.

[23] T. Koyaguchi, Grain-size variation of the tephra derived from umbrella clouds, Bull. Volcanol. 56 (1994) 1–9.

[24] T. Koyaguchi, M. Ohno, Reconstruction of the eruption column dynamics on the basis of grain size of tephra fall deposits. 1. Metods, J. Geophys. Res. 106 (B4) (2001) 6499–6512.

[25] J. Heffter, B. Stunder, Volcanic Ash Forecast Transport and Dispersion (Vaftad) model, Weather Forecast. 8 (1993) 533–541.

[26] R. D'Amours, Modeling the ETEX plume dispersion with the Canadian emergency response model, Atmos. Environ. 32 (24) (1998) 4335–4341.

[27] C. Searcy, K. Dean, W. Stringer, Puff: a high-resolution volcanic ash tracking model, J. Volcanol. Geotherm. Res. 80 (1998) 1–16.

[28] S. Reynolds, P. Roth, J. Seinfeld, Mathematical modeling of photochemical air pollution. I. Formulation of the model, Atmos. Environ. 7 (1973) 1033–1061.

[29] O. Toon, R. Turco, D. W., R. Malone, M. Liu, A multidimensional model for aerosols: description of computer analogs, J. Atmos. Sci. 45 (1988) 2123–2143.

[30] M. Jacobson, R. Lu, R. Turco, O. Toon, Development and application of a new air pollution modeling system. Part I: gas-phase simulations, Atmos. Environ. 30 (1996) 1939–1963.

[31] S. Park, C. Kim, A numerical model for the simulation of SO_2 concentrations in the Kyongin region, Korea, Atmos. Environ. 33 (1999) 3119–3132.

[32] D. Byun, J. Chin, in: D.W. Byun, J.K.S. Chin (Eds.), Science Algorithms of the EPA Model-3 Community Multiscale Air Quality (CMAQ) Modeling System, vol. III, U.S. Environmental Protection Agency, Washington, DC, 1999, EPA-600/R-99-030.

[33] W. Cornell, S. Carey, H. Sigurdsson, Computer simulation and transport of the Campanian Y-5 ash, J. Volcanol. Geotherm. Res. 17 (1983) 89–109.

[34] G. Grell, J. Dudhia, D. Stauffer, A Description of the Fifth-Generation Penn State/NCAR Mesoscale Model (MM5), Technical Report NCAR/TN-398+STR, National Center for Atmospheric Research, Boulder, Colorado, June 1994.

[35] R. Pielke, W. Cotton, R. Walko, C. Tremback, M. Nicholls, M. Moran, D. Wesley, T. Lee, J. Copeland, A comprehensive meteorological modeling system-RAMS. Meteor, Atmos. Phys. 49 (1992) 69–91.

[36] J. Scire, F. Robe, F. M.E., R. Yamartino, A User's Guide for the CALMET Meteorological Model. Tech. Rep. Version 5, Earth Tech, Inc., 196 Baker Avenue, Concord, MA 01742, 2000.

[37] J. Dutton, G. Fichtl, Approximate equations of motion for gases and liquids, J. Atmos. Sci. 26 (1969) 241–254.

[38] J. Sang, G. Lin, B. Zhang, Numerical modeling for emergency response of nuclear accident, J. Wind Eng. Ind. Aerodyn. 81 (1999) 221–235.

[39] L. Nance, D. Durran, A comparison of the accuracy of three anelastic systems and pseudo-incompressible system, J. Atmos. Sci. 51 (1994) 3549–3565.

[40] D. Byun, Dynamically consistent formulations in meteorological and air quality models for multiscale atmospheric studies. Part I: governing equations in a generalized coordinate system, J. Atmos. Sci. 56 (21) (1999) 3789–3807.
[41] D. Byun, Dynamically consistent formulations in meteorological and air quality models for multiscale atmospheric studies. Part II: mass conservation issues, J. Atmos. Sci. 56 (21) (1999) 3808–3820.
[42] M. Jacobson, Fundamentals of Atmospheric Modelling, 1st edition, Cambridge University Press, New York, 1999.
[43] A. Ulke, New turbulent parameterization for a dispersion model in atmospheric boundary layer, Atmos. Environ. 34 (2000) 1029–1042.
[44] W. Collins, P. Rasch, B. Boville, J. Hack, J. McCaa, D. Williamson, J. Kiehl, B. Briegleb, Description of the NCAR Community Atmosphere Model (CAM 3.0). Technical Report NCAR/TN-464+STR, National Center for Atmospheric Research, Boulder, Colorado, 2004.
[45] R. Pielke, A three dimensional numerical model of the sea breezes over south Florida, Mon. Weather Rev. 102 (1974) 115–139.
[46] R. Pielke, Mesoscale Meteorological Modeling, Academic Press, New York, 1984, p. 612.
[47] W. Physick, Mesoscale modeling of a cold front and its interaction with a diurnally heated land mass, J. Atmos. Sci. 45 (1988) 3169–3187.
[48] Z. Boybeyi, S. Raman, Simulation of elevated long-range plume transport using a mesoscale meteorological model, Atmos. Environ. 29 (1995) 2099–2111.
[49] A. Azad, T. Kitada, Characteristic of the air pollution in the city of Dhaka, Bangladesh in winter, Atmos. Environ. 32 (1998) 1991–2005.
[50] T. Pfeiffer, A. Costa, G. Macedonio, A model for the numerical simulation of tephra fall deposits, J. Volcanol. Geotherm. Res. 140 (2005) 273–294.
[51] R. Chhabra, L. Agarwal, N. Sinha, Drag on non-spherical particles: an evaluation of available methods, Powder Technol. 101 (1999) 288–295.
[52] G. Walker, L. Wilson, E. Bowell, Explosive volcanic eruptions. I. Rate of fall of pyroclasts, Geophys. J. R. Astron. Soc. 22 (1971) 377–383.
[53] L. Wilson, T. Huang, The influence of shape on the atmospheric settling velocity of volcanic ash particles, Earth Planet. Sci. Lett. 44 (1979) 311–324.
[54] G. Ganser, A rational approach to drag prediction spherical and non-spherical particles, Powder Technol. 77 (1993) 143–152.
[55] G. Macedonio, A. Costa, A. Longo, A computer model for volcanic ash fallout and assessment of subsequent hazard, Comput. Geosci. 31 (7) (2005) 837–845.
[56] G. Ernst, R. Sparks, S. Carey, M. Bursik, Sedimentation from turbulent jets and plumes, J. Geophys. Res. 101 (B3) (1996) 5575–5589.
[57] D. Pyle, The thickness, volume and grainsize of tephra fall deposits, Bull. Volcanol. 51 (1989) 1–15.
[58] R. Ewing, H. Wang, A summary of numerical methods for time-dependent advection-dominated partial differential equations, J. Comput. Appl. Math. 128 (2001) 423–445.
[59] P. Sweeby, High resolution schemes uning flux limiter for hyperbolic conservation laws, SIAM J. Numer. Anal. 21 (5) (1984) 995–1011.
[60] Y. Wang, K. Hutter, Comparisons of numerical methods with respect to convectively dominated problems, Int. J. Numer. Methods Fluids 37 (2001) 721–745, doi:10.1002/fld.197.
[61] A. Hindmarsh, P. Gresho, D. Griffiths, The stability of explicit Euler integration for certain finite difference approximations of the multidimensional advection–diffusion equation, Int. J. Numer. Methods Fluids 4 (1984) 853–897.
[62] S. Scollo, P. Del Carlo, M. Coltelli. Tephra fallout of the July–August 2001 Etna eruption: deposit features and analysis of plume dispersion. J. Volcanol. Geotherm. Res (submitted for publication).
[63] C. Bonadonna, B. Houghton, Grain-size distribution and volume of tephra-fallout deposits, Bull. Volcanol. 67 (2005) 441–456, doi:10.1007/s00445-004-0386-2.
[64] T. Mather, D. Pyle, C. Oppenheimer, Tropospheric volcanic aerosol, in: R. Scarpa, R. Tilling (Eds.), Volcanism and the Earth's Atmosphere. No. 139 in Geophysical Monograph, American Geophysical Union, Washington D.C., 2003, pp. 189–212.
[65] W. Rose, G. Bluth, D. Schneider, G. Ernst, C. Riley, L. Henderson, R. McGimsey, Dispersal of ash in the great Toba eruption, 75 ka, J. Geol. 109 (2001) 677–694.
[66] S. Barsotti, A. Neri, J. Scire. Forecasting volcanic ash dispersal: developments and applications of the system Calpuff (in preparation).
[67] C. Bonadonna, C. Connor, B. Houghton, L. Connor, M. Byrne, A. Laing, T. Hincks, Probabilistic modeling of tephra dispersal: hazard assessment of a multiphase rhyolitic eruption at Tarawera, New Zealand, J. Geophys. Res. 110 (2005), doi:10.1029/2003JB002896.